ENVIRONMENTAL NOISE IN GRAVITATIONAL WAVE DETECTORS AND

THE SEARCH FOR GRAVITATIONAL WAVE SIGNALS ASSOCIATED

WITH GAMMA-RAY BURSTS DURING LIGO'S THIRD OBSERVING RUN

by

PHILIPPE DAI-QUANG NGUYEN

THIS IS A DRAFT COPY FOR REVIEW AND EDITING PURPOSES ONLY!

This draft format in no way complies with the University of Oregon Style Graduate School Style Guide for theses or dissertations. This draft may employ 10 point fonts for paper conservation, line numbering for ease of editing, or watermarking and editing notations; all of which violate the Graduate School Style Guide for final documents. See the uothesis.cls documentation for instructions on producing a properly formatted document.

A DISSERTATION

Presented to the Department of Physics
and the Division of Graduate Studies of the University of Oregon
in partial fulfillment of the requirements
for the degree of
Doctor of Philosophy

Month 2021

LaTeX

DISSERTATION ABSTRACT

Philippe Dai-Quang Nguyen

Doctor of Philosophy

Department of Physics

Month 2021

Title: ENVIRONMENTAL NOISE IN GRAVITATIONAL WAVE DETECTORS
AND THE SEARCH FOR GRAVITATIONAL WAVE SIGNALS ASSOCIATED
WITH GAMMA-RAY BURSTS DURING LIGO'S THIRD OBSERVING RUN

My abstract goes here.

CURRICULUM VITAE

NAME OF AUTHOR: Philippe Dai-Quang Nguyen

GRADUATE AND UNDERGRADUATE SCHOOLS ATTENDED:

University of Oregon, Eugene, OR, USA
California Polytechnic State University, San Luis Obispo, CA, USA

DEGREES AWARDED:

Doctor of Philosophy, Physics, 2022, University of Oregon
Bachelor of Science, Physics, 2016, Cal Poly San Luis Obispo

AREAS OF SPECIAL INTEREST:

Gravitational Wave Astrophysics

PROFESSIONAL EXPERIENCE:

Research Assistant, Department of Physics, University of Oregon, 2017-
present
Teaching Assistant, Department of Physics, University of Oregon, 2016-
2019

GRANTS, AWARDS AND HONORS:

LIGO Scientific Collaboration Fellow, LIGO Hanford Observatory, 2017

PUBLICATIONS:

Nguyen, P., et al. (2021). Environmental noise in Advanced LIGO
detectors. *Classical Quantum Gravity*, 38(14), 145001.

Davis, D., et al. (2021). LIGO detector characterization in the second and third observing runs. *Classical Quantum Gravity*, 38(13), 135014.

TABLE OF CONTENTS

LIST OF FIGURES

LIST OF TABLES

CHAPTER I

INTRODUCTION

1.1 Gravitational waves

To develop theory of gravitational waves (GWs), we begin with the Einstein field equations

$$G_{\mu\nu} = \frac{8\pi G}{c^4} T_{\mu\nu}$$

where $T_{\mu\nu}$ is the stress-energy tensor and $G_{\mu\nu} = R_{\mu\nu} - \frac{1}{2} R g_{\mu\nu}$ is the Einstein tensor, comprised of the Ricci tensor $R_{\mu\nu}$, Ricci scalar R, and spacetime metric $g_{\mu\nu}$. We can approximate the solution as the flat Minkowski metric $\eta_{\mu\nu}$ plus a perturbation $h_{\mu\nu}$: $g_{\mu\nu} = \eta_{\mu\nu} + h_{\mu\nu}$. Assuming the perturbation is small $|h_{\mu\nu}| \ll 1$, we can construct the linearized Ricci tensor

$$R_{\mu\nu} = \frac{1}{2}(\partial_\sigma \partial_\mu h_\nu^\sigma + (\mu \leftrightarrow \nu) - \partial_\mu \partial_\nu h - \Box h_{\mu\nu})$$

where $h = \eta^{\mu\nu} h_{\mu\nu}$ is the trace of $h_{\mu\nu}$, and the linearized Ricci scalar

$$R = \eta_{\mu\nu} R^{\mu\nu} = \partial_\mu \partial_\nu h - \Box h_{\mu\nu}$$

This yields the linearized Einstein tensor

$$G_{\mu\nu} = \frac{1}{2}\left(\partial_\mu \partial_\sigma \bar{h}_\nu^\rho + (\mu \leftrightarrow \nu) - \eta^{\sigma\rho} \partial_\sigma \partial_\rho \bar{h}_{\mu\nu} - \eta_{\mu\nu} \partial_\sigma \partial_\rho \bar{h}^{\sigma\rho}\right)$$

where $\bar{h}_{\mu\nu} := h_{\mu\nu} - \frac{1}{2}\eta_{\mu\nu} h$ is the trace-reversed metric perturbation.

We can simplify these terms further by choosing the appropriate gauge. The Lorenz, or harmonic, gauge allows us to drop the terms containing the

divergence of $\bar{h}_{\mu\nu}$. In this gauge we fix $\partial_\mu \bar{h}^{\mu\sigma} = 0$, reducing the linearized Einstein field equations to simply

$$-\Box \bar{h}_{\mu\nu} = \frac{8\pi G}{c^4} T_{\mu\nu} \tag{1.1}$$

In the Newtonian (slowly-varying) limit, the D'Alembertian operator becomes a spatial Laplace operator, and it can be shown that the trace-reversed perturbation reduces to the Newtonian gravitational potential Φ and the stress-energy tensor reduces to just the mass density, recovering the Poisson equation for Newtonian gravity: $\nabla^2 \Phi = 4\pi G \rho$.

In vacuum, the field equation is simply $\Box \bar{h}_{\mu\nu} = 0$, the solution to which is a GW propagating at the speed of light: $\bar{h}_{\mu\nu} = A_{\mu\nu} \cos(k_\sigma x^\sigma - \phi_{\mu\nu})$, where $A_{\mu\nu}$ and $\phi_{\mu\nu}$ are the amplitude and phase of the wave.

In the slowly-varying case the gauge condition can be further restricted by making the metric perturbation purely spatial, ($h_{00} = h_{0i} = 0$) and traceless ($h = h_i^i = 0$). In this transverse-traceless (TT) gauge, we write the metric perturbation as $h_{\mu\nu}^{TT}$ (no overline necessary because trace-reversal has no effect on the traceless perturbation). The gravitational wave described by $h_{\mu\nu}^{TT}$ is transverse to its direction of propagation. These gauge conditions cause all components to vanish except two independent ones. For a monochromatic plane wave propagating in the z direction, these two components are

$$h_{11}^{TT} = -h_{22}^{TT} = h_+(t-z)$$

$$h_{12}^{TT} = h_{21}^{TT} = h_\times(t-z)$$

and are called the plus and cross polarizations, respectively. The effect of these polarizations on an array of test particles is a stretching and compressing of the distances between the particles in the xy plane.

The general solution to (1.1) is analogous to the problem of solving for the vector potential given a source current, where here we solve for the metric perturbation given a stress-energy tensor describing the gravitational wave source. The result is an integral of the stress-energy tensor:

$$\bar{h}_{\mu\nu}(t, \vec{x}) = \frac{4G}{c^4} \int \frac{T_{\mu\nu}(t - \|\vec{x} - \vec{x}'\|/c, \vec{x}')}{\|\vec{x} - \vec{x}'\|} d^3x'$$

If the source is slowly moving and the gravitational wave energy is small, the solution can be simplified to

$$h_{ij}^{TT}(t, \vec{x}) \simeq \frac{2G}{c^4 r} \ddot{I}_{ij}^{TT}(t - r/c) \tag{1.2}$$

where I_{ij}^{TT} is the transverse-traceless projections of the quadrupole moment tensor of the source, $I_{ij}(t) = \int x_i x_j \rho(t, \vec{x}) d^3x$.

1.2 Sources of gravitational waves

Eq. 1.2 shows that any system whose quadrupole moment has a non-vanishing second derivative can generate GWs, which requires some non-spherically symmetric motion of masses. The frequency of the waves is determined by the motion, usually some rotational frequency, of the masses. Generating strong waves requires high masses and speeds, so it is reasonable to look for GWs from astrophysical sources.

The simplest example is a binary system of massive, compact objects, such as neutron stars (NSs) or black holes (BHs). For most of their lifetime, the binary generates continuous GWs at a more-or-less steady frequency twice the orbital frequency of the components. Over time, the orbit decays due to the loss of energy to GW emission, causing the frequency and amplitude of the emission to increase. The time evolution scales with the component masses, so highly massive binaries, e.g. binary black hole (BBH) systems, generate gravitational waves that sweep up in frequency and amplitude more quickly than less massive ones, e.g. binary neutron star (BNS) and neutron star-black hole (NSBH) systems. These compact binary coalescences (CBCs) creates a distinct GW signature, characterized by a short-duration (< 1 s for BBHs, ~ 100 s for BNSs), high frequency ($\sim 10 - 1000$ Hz) chirp. These violent merger events happen very frequently, making them the best candidate for detecting gravitational waves with existing detectors.

Continuous GWs generated from binary systems range from very low frequency ($\sim$ nHz) waves from supermassive BH binaries, to $\sim$ mHz waves from stellar-mass galactic binaries, but in higher frequency bands the best candidates are isolated, rapidly rotating NSs (Riles, 2017). If such an NS exhibits any asymmetry with respect to its rotational axis, it generates GWs at twice its rotational frequency.

Burst sources of GWs are short duration events not generated by binary mergers; their time evolution is too difficult to model due to their unpredictable or poorly understood dynamical behavior. Core-collapse supernovae are the most promising source to be detected, but their GW emission is still expected to be

too weak for detecting events outside the galactic neighborhood. Other potential sources include magnetar flares and cosmic string cusps.

The superposition of all GWs forms a stochastic GW background analogous to the cosmic microwave background (CMB) (Christensen, 2018). This background is comprised of stellar-mass binary BH and NS mergers at frequencies currently observable by GW detectors, but at lower frequencies galactic white dwarf binaries and supermassive BH mergers would also contribute to the stochastic background. At cosmological distances, relic gravitational waves from the very early universe could be detectable via their effect on the polarization of the CMB radiation.

Thus far, XX gravitational wave signals originating from CBCs have been detected by existing GW detectors (R. Abbott et al., 2021b). Of these, the vast majority, XX, originated from the mergers of BBHs, XX from BNSs, and XX from NSBHs. There has yet to be a detection of a GW signal with a significant probability of having a non-CBC origin.

CHAPTER II

GRAVITATIONAL WAVE DETECTORS

Detection of gravitational waves requires measuring the transverse stretching and compressing of space. The earliest attempt at this was done through resonant mass detectors, solid, vibrationally isolated cylinders tuned to a particular frequency that could be used to detect the effect of gravitational waves on the length of the cylinders. These proved incapable of reaching the required sensitivity for detecting even the strongest gravitational waves in the frequency band they were designed for (~ 1 kHz).

The current era of GW detection is dominated by laser interferometers inspired by the simple Michelson interferometer. There are currently three observatories in operation: the Laser Interferometer Gravitational-Wave Observatory (LIGO), consisting of LIGO Hanford Observatory (LHO) in Washington and LIGO Livingston Observatory (LLO) in Louisiana, and the Virgo observatory in Italy. Additional detectors in Japan (Kagra) and India (LIGO India) are under construction, and projects for next-generation detectors (Einstein Telescope, Cosmic Explorer, and the Laser Interferometer Space Antenna (LISA)) are on the horizon.

A GW interferometer is configured so that the anti-symmetric output port (the output not leading back to the laser source) observes no signal due to destructive interference. If one interferometer arm is elongated relative to the other, the phase shift between the signals from both arms results in some constructive interference; thus the amplitude of a gravitational wave passing through the plane of the detector arms is converted to an amplitude in laser light measured at the output port. Sensitivity scales with interferometer arm

length, but the incredible length required to detect gravitational waves from even the loudest sources (100s of km in order to observe black hole binary mergers) makes this infeasible. However, the effective arm length can be increased by making the arms Fabry-Perot cavities, so that light travels many (~ 300) times back and forth in each arm before leaving through the beam splitter.

Other methods that have been implemented to dramatically improve the sensitivity current-generation of Advanced LIGO (aLIGO) and Advanced Virgo include increasing laser power or injecting squeezed light to reduce the effects of photon shot noise; implementing a power recycling cavity at the symmetric output that sends the constructively-interfering light leaving in that direction back into the interferometer; implementing a signal recycling cavity at the anti-symmetric output to tune the most sensitive frequency band of the detector; larger mirrors to combat radiation pressure on the mirrors due to high laser power (Creighton & Anderson, 2011).

The two LIGO detectors began the first observing run (O1) on September 12, 2015, and made the first detection of a GW from a BBH merger on September 14, 2015 (Abbott et al., 2016b). This was followed by two more BBH detections before the end of the run on January 16, 2016 (B. P. Abbott et al., 2019). The second observing run (O2) began on November 30, 2016 after a period of detector upgrades and ended on August 25, 2017. During that run, in addition to several more BBH detections, the LIGO network (with the addition of Virgo towards the end of the run) observed the first BNS merger on August 17, 2017 (B. P. Abbott et al., 2017). The third observing run (O3), which spanned April 1, 2019 to March 27, 2020, came after another round of major improvements in the performance of the detectors (Buikema et al., 2020)

and the full inclusion of the Virgo detector in the GW network. Throughout O3, LIGO and Virgo observed a total of XX GW events (R. Abbott et al., 2021a, 2021b).

CHAPTER III

METHODS FOR STUDYING ENVIRONMENTAL NOISE

First three sections here are mostly copied verbatim from PEM paper. I think this needs to be split into multiple chapters. Not sure how though.

Environmental noise refers to any signal originating from outside the structure of a GW detector that can impact the detector's sensitivity or disrupt its ability to achieve and maintain lock (Effler et al., 2015; Nguyen et al., 2021). The effects of environmental noise on detector sensitivity can range from persistent excess noise in the GW strain data, to short-duration transient signals, or *glitches*.

One goal of studying environmental noise is to aid in the validation of GW events. Due to the sophisticated nature of the search pipelines used to detect gravitational waves in the LIGO data, environmental glitches are highly unlikely to fully account for a GW event candidate. That said, glitches capable of influencing analyses occur frequently at both observatories.

Unlike instrumental noise, environmental noise can potentially be correlated between different detectors, i.e. stemming from a common source as opposed to stemming from chance coincidence. Such correlated noise is not accounted for in the estimation of false-alarm probabilities, which is done by time-shifting background data from each LIGO detector to produce long stretches of coincident background.

Environmental noise is particularly important in searches for un-modeled sources of gravitational waves, as these look for excess power without the use of waveform templates. Even for highly significant CBC events, contamination of the strain data can be detrimental to parameter estimation analyses that

infer source properties from the morphology of the event. Thus it is important to have a quantitative solution for identifying and evaluating the impact of environmental transients when they occur coincide with candidate events.

The second goal is to improve the sensitivity and performance of the detector by localizing noise sources and coupling mechanisms. Once tracked down, they can be mitigated by eliminating the noise sources, attenuating the propagation of the signal, or modifying the detector itself.

3.1   Sources of environmental noise

The environment can influence a GW detector through physical contact (via vibrations or temperature fluctuations), electromagnetic waves, static electric and magnetic fields, and possibly high-energy radiation.

Vibrations can affect the data by directly moving the test masses. They can also cause modulate the paths of light that is scattered off of surfaces inside the interferometer, or introduce fluctuations in the alignment of the input laser beam.

3.2   The PEM sensor array

Understanding environmental influences on the detectors requires comprehensive monitoring of its physical surroundings. This is done through the physical environmental monitoring (PEM) system of auxiliary sensors (Figure 1), which consists of accelerometers for high-frequency vibrations (between tens to thousands of Hertz), seismometers for low-frequency vibrations (up to tens of Hertz), microphones, magnetometers, voltage monitors that measure the voltage of electric power supplied to the detector sites, radio-frequency (RF)
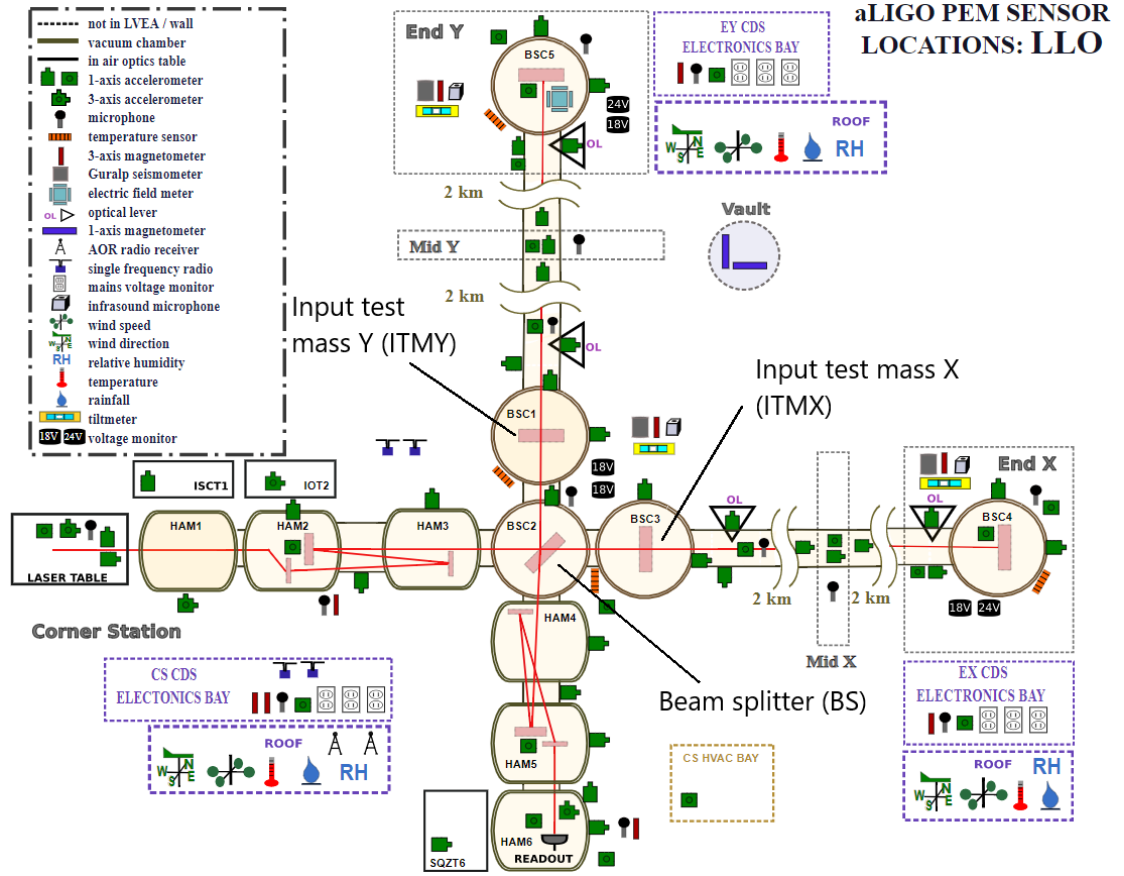
Figure 1. The PEM system layout at LLO during O3, as seen on the PEM public website.

receivers, a cosmic-ray detector for high-energy particles, and wind, temperature and humidity sensors. Detailed information on PEM sensors, including example background spectra and calibration data, can be found on the PEM website, PEM.LIGO.org (R. Schofield, Effler, Nguyen, et al., 2021).

3.3 Tests of environmental coupling

The effect of environmental influences on the sensitivity of a GW detector can be studied by making noise *injections*. These are signals produced by human-operated sources with the intention of replicating environmental

Figure 2. Standard locations for vibration and magnetic injections at the LHO corner station (left), Y end station (top right), and X end stations (bottom right).

disturbances with sufficient amplitude to produce excess noise in the differential arm length (DARM) spectrum. The amplitude of the excess, combined with measurements of the input signal, can be used to quantify the coupling behavior (Section 3.4). The most common examples are acoustic injections, generated using speakers, seismic injections generated by vibrational shakers, and magnetic field injections generated by electrical current loops.

At each observatory we inject from 13 locations with acoustic injections, about 12 with shaking injections, and 15 with small-coil magnetic injections, with 7 large-coil magnetic injection locations planned for the fourth observing run (O4) (as explained in Section 3.3.2). The number and locations of shaker injections vary between injection campaigns. For all injection types, multiple

injections are made at each location in order to focus on different frequency bands. Additionally, impulse injections (not shown) are made at locations where vibrational injections have revealed strong coupling sites.

Table 1. Specifications for injection equipment.

Equipment	Injection type
Custom enclosure with two 14-in. speakers	Acoustic
Various smaller speakers	Acoustic
APS 113 Electro-Seis®Long Stroke Shaker (APS Dynamics, 2014)	Vibrational
Piezosystem® (Piezosystems, n.d.) shaker with custom reaction mass	Vibrational
Brüel & Kjær® (Brüel & Kjær, 2021) EM shaker with custom reaction mass	Vibrational
1 m diameter copper coil (100 turns)	Magnetic
3 x 3 m and 5 x 5 m coils (80-100 turns)	Magnetic

Injection locations are chosen to best mimic disturbances from outside the detector (Figure 2). To do so we choose them to be as far from the detector and environmental sensors as possible, but we are usually limited by the size of the detector sites themselves (some injections can be made from outside). Time dedicated to these tests has to be balanced against other instrumental work and observing time, which leads to a trade-off between measurement uncertainty and coverage. We perform injections from as many locations as time allows in order to maximize coverage of potential coupling sites. Increased time allocation toward environmental studies in recent years has allowed for a significant increase in the number of injection locations. Table 1 summarizes the current equipment used and Figure 3 shows photos of some of the equipment.

Figure 3. Injection equipment photos. From left to right: wall-mounted magnetic field injection coil; 14-in. speakers; APS 113 shaker connected to the door of a vacuum chamber by a rigid fiberglass rod; modified Piezosystem shaker clamped to an electronics rack; modified B&K shaker clamped to a beam tube support.

3.3.1   Vibrational injections

Acoustic injections are produced by large speakers. For the corner stations, a pair of speakers mounted on a vibrationally isolated cart (to minimize ground-based vibrational signals) are used. Typically, the injection signal is white noise band-passed between 20-2000 Hz, with narrower bands being used for special follow-up of particular coupling sites.

Seismic injections at low frequency (up to tens of Hertz) during Initial LIGO (iLIGO) were performed with small electromagnetic and piezoelectric shakers and a weighted cart. A large shaker has been used since the beginning of noise studies for O3. The large shaker can impart up to 133 N of sine force and a peak-to-peak displacement of 158 mm (APS Dynamics, 2014), compared to the electromagnetic shaker which imparts up to 45 N of force and a displacement of 8 mm (Brüel & Kjær, 2021). While smaller shakers can be directly clamped to the interferometer supports, a rigid fiberglass rod is used to connect the large shaker to the interferometer. This has an added benefit of being better able to adjust the direction of the actuation by angling the rod and shaker accordingly.

Two new injection techniques have been developed for localizing vibration coupling sites connected to the vacuum enclosure, such as locations on the vacuum enclosure that reflect scattered light. The techniques rely on the slow propagation speeds (hundreds of meters per second) of vibrations on the steel vacuum enclosure walls or, for acoustic injections, in air. These two techniques aided in the localization of a coupling site that was producing a $48\,\mathrm{Hz}$ peak in the GW channel throughout the first half of O3, as discussed in Section **??**.

3.3.1.1 *Beating-shakers technique.* The beating-shakers technique is narrow-band, and involves vibrating the vacuum enclosure at two slightly different frequencies, each injected from a shaker or a speaker at a different location (e.g. a shaker at one location injects a sine wave at frequency f and a shaker at the other location injections at frequency $f + 0.01\,\mathrm{Hz}$). The two injections are adjusted in amplitude to produce strong beats in the GW channel.

Because the injection locations are different, the relative phase of the two injected signals varies with location on the vacuum enclosure. As a result, the phase of the beat envelope varies with position, and different sites experience maximum chamber wall motion at different times. The sites with accelerometer signals that have the same beat envelope phase as the DARM signal are candidates for the scattering sites on the vacuum enclosure walls. Other sensors that are not near the coupling site may also match the phase by chance, but these false positives can be rejected by varying the locations of the shakers.

3.3.1.2 *Impulse injections.* The second injection technique, which is broad band, involves propagation delays in impulse injections. Impulse injections are performed by striking the vacuum enclosure directly with enough force to produce a transient in the GW channel and in nearby accelerometers. The

vibrational impulse propagates through the structure of the vacuum enclosure, arriving at different accelerometers and coupling sites at different times.

We can distinguish these arrival times because the propagation velocity is much slower than in solid material, and is only roughly 300 m/s in our case. Using time series plots, the arrival time of the impulse in the GW channel is compared to the arrival time of the impulse in multiple accelerometers. The accelerometers that show the same arrival time as in the GW channel are more likely to be near a coupling site than those that observe the impulse much earlier or later. Again, varying the location of the injection eliminates sensors that match the detector time-of-arrival by chance but are actually far from the coupling site.

An additional consistency check is that the coupling of accelerometers near the coupling site will vary less between different impulse locations than that of accelerometers far from the coupling site. Finally, if the accelerometer is at the coupling site, the impulse in the GW channel will have a resonance structure that is similar to the resonance structure of the accelerometer signal, which can be judged from spectrograms.

3.3.2 Magnetic injections

Improvements have also been made to the magnetic field injection equipment. In order to generate fields strong enough to couple into the GW channel using the 1 m magnetic field coils built during iLIGO, we must focus the power of the coil into narrow bands and combs instead of injecting broadband signals. This was sufficient in iLIGO when strong magnetic coupling occurred primarily through permanent magnets. However, due to the removal

of permanent magnets from the test masses, coupling from those sources has decreased and cables and connectors have become the dominant coupling sites above about $80\,\mathrm{Hz}$, introducing more structure to the coupling functions and requiring stronger injections.
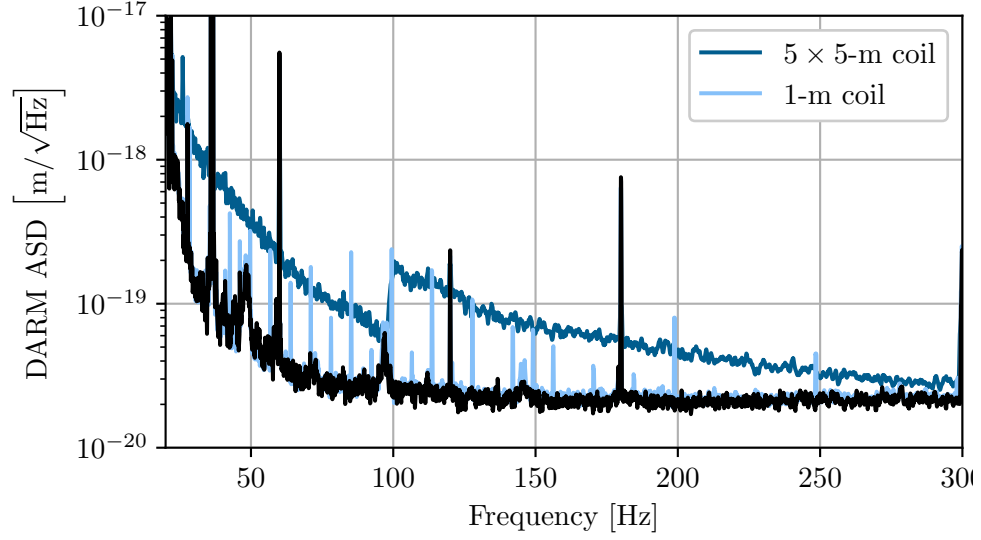
Figure 4. Comparison of the old small-coil comb magnetic field injections with the new large-coil broadband injections.

To achieve high-amplitude broadband magnetic injections, seven wall-mounted coils, each one a $3\,\mathrm{m}$ x $3\,\mathrm{m}$ or $5\,\mathrm{m}$ x $5\,\mathrm{m}$ square of 80-100 turns, are being installed at each site; three at the corner station and two at each end station. These coils are fixed in place and can be operated remotely, allowing for weekly injections to monitor variations in magnetic coupling caused by changes to electronics. Figure 4 compares the old and new magnetic injections. Some coils were installed and operated at the sites during O3; the project will be completed by the start of O4.

3.4 Coupling functions

3.4.1 Single coupling site, sensor, and injection

Suppose there exists exactly one coupling site, i.e. one location at which incident environmental signals result in excess noise in the GW strain data. Suppose also that a sensor is placed at the location of the coupling site, and a noise injection is performed that produces a signal observable by the sensor and the interferometer readout. The coupling mechanism can be modeled in the frequency domain as a linear system:

$$h(f) = C(f)x(f), \tag{3.1}$$

where $h(f)$ is the amplitude spectral density (ASD) of the detector (strain) response, x is the ASD of the injection signal as measured by the sensor, and $C(f)$ is the *coupling function*, which represents the amplitude of gravitational wave strain noise per unit amplitude in the sensor. By convention, the strain is typically converted to DARM, in meters, in which case $C(f)$ represents test mass displacement per unit of sensor amplitude. If the injection signal is an acoustic signal and the sensor is a microphone measuring amplitude in Pa, for instance, then the acoustic coupling function is in units of m/Pa.

In both the witness sensor and the detector, some ambient background noise is always present whether or not an injection is produced. Let $h_{\mathrm{bkg}}(f)$

and $h_{\mathrm{inj}}(f)$ be the ASDs of the detector during a period of background noise and during the injection, respectively. Likewise let $x_{\mathrm{bkg}}(f)$ and $h_{\mathrm{inj}}(f)$ be the background and injection ASDs of the sensor. Since the noise adds linearly in the power spectral domain, the actual signal in each is the difference between the injection-time and background-time power spectral densities (PSDs):

$$[h(f)]^2 = [h_{\mathrm{bkg}}(f)]^2 - [h_{\mathrm{bkg}}(f)]^2 \tag{3.2}$$

$$[x(f)]^2 = [x_{\mathrm{bkg}}(f)]^2 - [x_{\mathrm{bkg}}(f)]^2 \tag{3.3}$$

Combining eqs. (3.1)–(3.3), we can measure the coupling function from the background and injection ASDs (Kruk & Schofield, 2016; Nguyen, 2020):

$$\mathrm{C}(f) = \sqrt{\frac{[h_{\mathrm{inj}}(f)]^2 - [h_{\mathrm{bkg}}(f)]^2}{[x_{\mathrm{inj}}(f)]^2 - [x_{\mathrm{bkg}}(f)]^2}}. \tag{3.4}$$

The value of a coupling function at a single frequency bin is referred to as a *coupling factor*.

3.4.2 Multiple coupling sites, sensors, and injections

Suppose now there are multiple coupling sites, and a sensor is placed at the location of each site. The detector response to an environmental signal now becomes a linear combination of the sensor signals and their sensor-specific coupling functions:

$$h(f) = \sum_{j=1}^{m} \mathrm{C}_j(f) x_j(f), \tag{3.5}$$

Solving for the coupling function now would require producing multiple injections instead of just one, resulting in a system of n equations with m unknown coupling functions, where n and m are the numbers of injections and sensors, respectively:

$$h_i(f) = \sum_{j=1}^{m} C_j(f) x_{ij}(f).$$

(3.6)

Here $h_i(f)$ is the detector response during injection i, $x_{ij}(f)$ is the amplitude measured by sensor j during injection i, and $C_j(f)$ is the coupling function of sensor j. If $n = m$, eq. (3.6) could be solved to determine the coupling functions of all sensors.

Thus far it has been assumed that the witness sensors are placed precisely at the locations of the coupling mechanisms, but such perfect placement is not realistically feasible given that there are an unknown number of coupling sites at unknown locations. A sensor, even if it is near a coupling site, only measures the injection amplitude at its own location, not at the coupling location. Therefore, when using real-world sensors, eq. (3.3) is not exact, so eq. (3.4) does not exactly describe the coupling at the coupling site. Nevertheless, as explained above, sensors are distributed in order to maximize coverage of coupling sites and this has been sufficient for producing reliable coupling functions for all sensors, as discussed further in Section 3.5.

3.4.3   Solving the coupling equations

One hurdle remains in attempting to solve eq. (3.6). In practice, typically $n \; < \; m$ due to logistical constraints on the number of injections one could perform during a realistic time window, which makes the system

of equations underdetermined. Below are two approximation methods for determining $C_j(f)$ for all sensors.

Nearest-sensors approximation. One method of forcing $n = m$ is reducing the number of sensors in each each equation, by asserting $x_{ij}(f) = 0$ for sensors that are sufficiently far from the source of injection i. This can be done by ordering the sensors by distance from the injection source and applying the assertion to the $m - n$ farthest sensors. Issues can arise if there are sensors that are never near enough to any injection source, causing them to zeroed out for all injections; this requires that injections be distributed such that each sensor is near enough to at least one injection.

Nearest-injection approximation. Instead of solving eq. (3.6) in full, one can approximate $C_j(f)$ for each sensor independently of other sensors. Given a sensor j, eq. (3.4) can be repurposed by replacing x with x_{ij} and h with h_i to compute a single-injection "coupling function" $\mathcal{C}_{ij}(f)$ for each injection:

$$\mathcal{C}_{ij}(f) = \sqrt{\frac{[h_{i,\mathrm{inj}}(f)]^2 - [h_{i,\mathrm{bkg}}(f)]^2}{[x_{ij,\mathrm{inj}}(f)]^2 - [x_{ij,\mathrm{bkg}}(f)]^2}}. \tag{3.7}$$

The closer an injection is to a sensor i, the more accurately $\mathcal{C}_{ij}(f)$ approximates $C_j(f)$, since the detector response would be dominated by coupling near sensor j. Therefore one can construct the sensor coupling function by choosing at each frequency bin the coupling factor corresponding to the nearest injection, determined by the highest sensor amplitude (using the assumption that injection amplitudes are equivalent). That is, for a frequency f_k and a set of injections $\mathcal{I}$, one can measure the sensor amplitudes $\{x_{ij}(f_k) \mid i \in \mathcal{I}\}$, compute the single-injection coupling functions $\{\mathcal{C}_{ij}(f_k) \mid i \in \mathcal{I}\}$, and construct the approximate sensor coupling function

$$\widetilde{\mathrm{C}}_j(f_k) := \mathcal{C}_{lj}(f_k) \text{ where } l = \underset{i \in \mathcal{I}}{argmax}\,(x_{ij}(f_k)). \tag{3.8}$$

If the distribution of injection locations provides sufficient coverage of sensor locations, then $\widetilde{\mathrm{C}}_j(f) \approx \mathrm{C}_j(f)$. Shortcomings of this assumption are discussed in Section 3.5.

Figure 5 provides an example of a coupling function measurement for a pre-stabilized laser (PSL) acoustic injection. Figure 6 shows an estimated ambient noise based on an accelerometer coupling function constructed from five single-injection coupling functions. For simplicity only five injections were used to produce this example, however in practice the number of injections performed near a sensor can be much higher.

Due to hardware limitations it can be possible for an injection signal to be strong enough to produce excess noise in a sensor ASD but not in the GW detector ASD. For frequency bins where this is the case, an upper limit on $\mathcal{C}_{ij}(f_k)$ can be established by assuming, as a worst-case scenario, that all of the detector noise at that frequency is produced by the coupling alone

$$\mathcal{C}_{ij,\mathrm{UL}}(f) = \frac{h_{i,\mathrm{bkg}}(f)}{\sqrt{[x_{ij,\mathrm{inj}}(f)]^2 - [x_{ij,\mathrm{bkg}}(f)]^2}}. \tag{3.9}$$

The larger the injection amplitude, the better this upper limit can be constrained. The boundaries between measurements, upper limits, and null results are established by two ASD ratio thresholds: a sensor threshold and a detector threshold. Let $r_x := x_{ij,\mathrm{inj}}(f)/x_{ij,\mathrm{bkg}}(f)$ and $r_h := h_{i,\mathrm{inj}}(f)/h_{i,\mathrm{bkg}}(f)$ represent the injection signal-to-noise ratios if the sensor and GW detector ASDs, respectively. If $r_x \geq t_x$ and $r_h \geq t_h$, where t_x is the sensor threshold
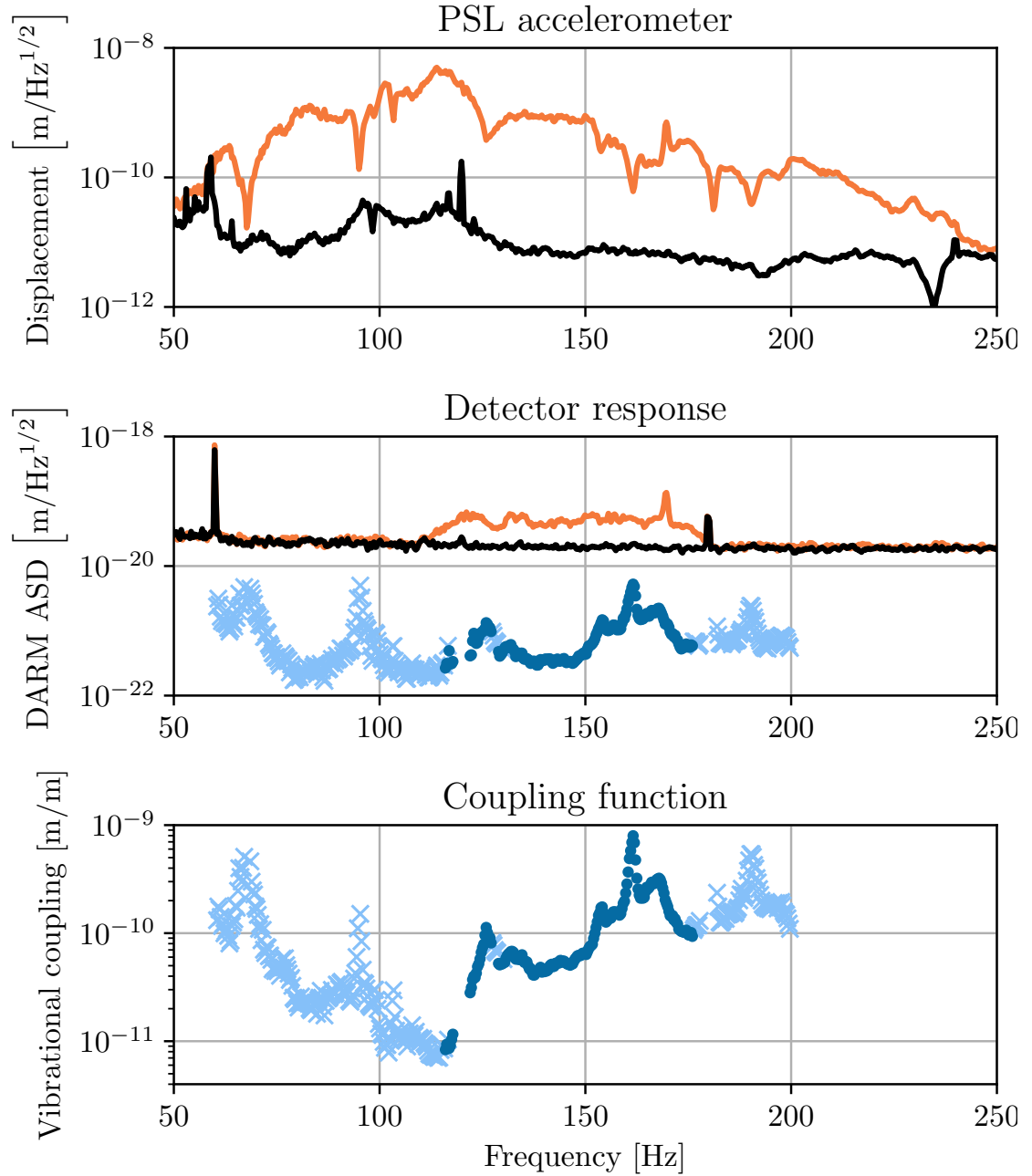
Figure 5. Example of a broadband acoustic noise injection and measurement of a single-injection coupling function. Top: displacement of an accelerometer in the PSL room during background time (black) and injection time (orange). Middle: DARM during background time (black) and injection time (orange). Estimated ambient levels for the accelerometer are shown as dark blue dots, with upper limits shown as light blue crosses. Bottom: single-injection coupling function used to produce estimated ambient above.

and t_h is the detector threshold, then a measurement is computed via eq. 3.7. Otherwise, if $r_x \geq t_x$ but $r_h < t_h$, then eq. 3.9 is used to place an upper limit on the coupling. If $r_x < t_x$ and $r_h < t_h$, then neither a measurement nor upper limit is computed. The null hypothesis is thus assumed:

$$\mathcal{C}_{ij,\text{null}}(f) = \frac{h_{i,\text{bkg}}(f)}{x_{i,\text{bkg}}(f)}. \tag{3.10}$$

The values of t_x and t_h are determined based on typical level of random fluctuations observed in the spectra, but often values of $t_x = 10$ and $t_h = 2$ are used for most types of sensors and injections. The higher choice of t_x is due to the environmental sensors being much more sensitive to random fluctuations in the ambient noise level than the interferometer is.

The coupling function as approximated in eq. 3.8 is used for comparing coupling between different sensor locations and producing estimates of interferometer noise levels, e.g. as part of event validation (see Section 4.3). References to a sensor's coupling function will hereafter refer to this approximate quantity. Figure 6 provides an example of an estimated ambient for an accelerometer on the HAM6 vacuum chamber (which houses the interferometer output optics). The PEM website provides coupling functions for all accelerometers, microphones, and magnetometers produced from the most recent campaign of injections (R. Schofield et al., 2021).
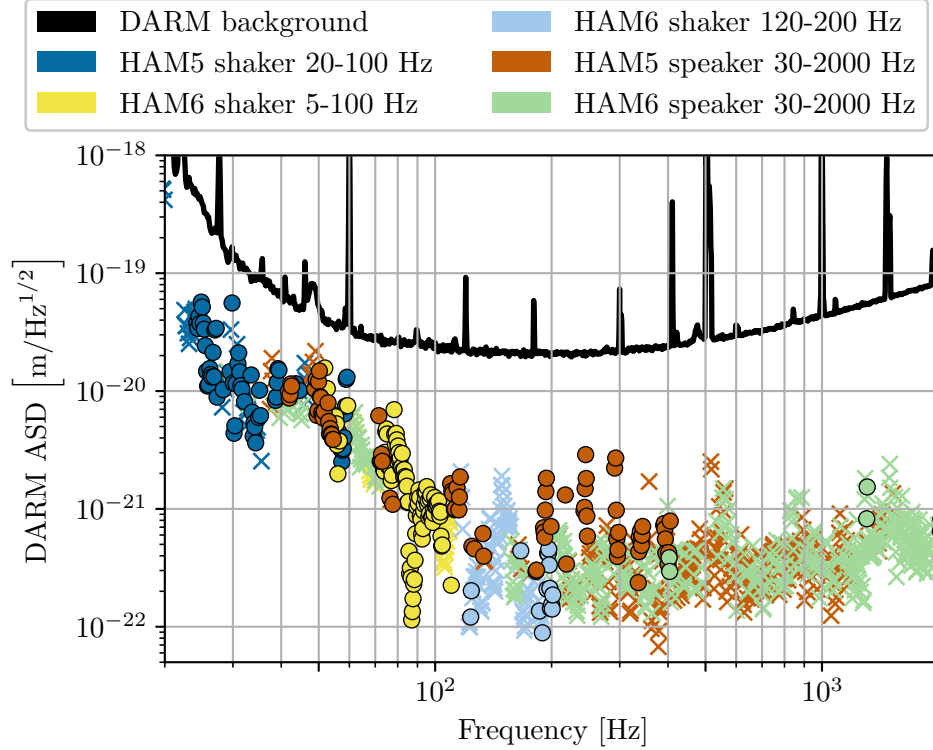
Figure 6. Ambient noise level for the LHO HAM6 Y-axis accelerometer estimated from a composite coupling function, using acoustic and seismic injections near the output arm.

3.5 Uncertainties and limitations of coupling functions

3.5.1 Comparison to transfer functions

Environmental coupling is characterized using coupling functions instead of transfer functions because perfect coherence is not assumed in the system. Low coherence can arise either due to non-linearity in the coupling or due to the spacing between the sensor and coupling site. On a superficial level, a coupling function lacks a phase response component, representing only the magnitude response in the system. Coupling functions also differ fundamentally from transfer functions in the sense that they do not assume the input signal to be

the true actuation signal, but rather merely a witness of the actuation, while the actuation is in fact occurring at the location of the true coupling site.

3.5.2   Assumptions about coupling mechanisms

Equation (3.4) relies on two assumptions about the coupling mechanism. First, the coupling is assumed to be linear in amplitude, e.g. doubling the amplitude of the injection would double the amplitude of the GW detector response. This is confirmed when performing injections by repeating them with different amplitudes and ensuring that the detector response scales proportionally with the injection amplitude. Second, the coupling function ignores any up- or down-conversion of the signal between the sensor and the GW detector. Such non-linear coupling can be very significant for scattering noise and bilinear coupling, but is not accounted for in the estimates of linear coupling. One way to check for non-linear coupling is by sweeping single frequency injections over time and searching for off-frequency responses in the GW detector. Frequency changes from non-linear coupling can be an issue in broadband injections where up- or down-converted noise in the interferometer readout appears in the injection band, resulting in artificially higher estimates at those frequencies. We split broadband injections into smaller frequency bands to avoid this effect when necessary. One approach for quantifying non-linear coupling is presented in Washimi et al. (2020).

3.5.3   Hardware limitations

Injection amplitudes. To measure coupling, we inject signals large enough to produce a response in the detector, but the maximum amplitude of injections

is limited by the sensitive range of the environmental sensors (saturation produces an overestimate of coupling). This effectively limits how far below the detector noise background we can probe for coupling or establish upper limits.

Recall that Eq. 3.8 was based on assuming that injection amplitudes are equivalent. However, this assumption is ambitious: since injections vary with distance to sensors, the amplitudes used have to be adjusted to achieve a large signals in the sensors and in the GW channel. This means that the highest-amplitude injection measured by a sensor is not necessarily the nearest injection to that sensor. If a further injection was performed using a much larger amplitude, its measured amplitude can trump that of a nearer injection, leading to the algorithm choose a more distant injection source location when determining $\widetilde{C}_j$. To prevent this issue, once $\mathcal{C}_{ij}$ is computed for all sensors for a single injection, an additional sensor threshold is applied that is a fraction of the highest amplitude observed by all sensors. This threshold is used only to demote measurements to upper limits. By doing so, this injection-dependent threshold vetos measurements produced by sensors that are far from the injection. For the O3 injections, the threshold was set at one third, meaning that a coupling measurement is demoted to an upper limit if the sensor measuring it observes the injection at less than a third of the amplitude observed by the sensor closest to the injection.

Need to talk about this a lot more. Injection-depended thresholding reflects a fundamental issue with the distribution of sensors and injections. In principle if you have many one-to-one correspondence b/w sensors and injections, you would just have each injection produce measurements in its nearest sensor, which is effectively what you get by setting this threshold to

Uncertainty due to injection locations. As mentioned above, the model in eq. (3.6) relies on the assumption that the environment is monitored at the coupling site. The density of sensors is not great enough for this to be strictly true, especially if the source of the environmental signal is closer to the coupling site than the sensor is. The detector response to an injection depends on the distance between the injection and coupling site, whereas the sensor response depends on the distance between the injection and sensor. Varying the injection location therefore varies the relative scaling of the numerator and denominator of eq. (3.7), affecting the measurement of $\mathcal{C}_{ij}(f)$ and subsequently the sensor coupling function via eq. (3.8). Therefore, a finite spacing of sensors leads to some degree of uncertainty in the coupling functions. This uncertainty also propagates to projected noise levels in the GW channel using these coupling functions.

Since the uncertainty manifests as a multiplicative scaling of $\mathcal{C}_{ij}(f)$, it can be described by computing a geometric standard deviation of $\mathcal{C}_{ij}(f)$ for a single sensor over a range of injection locations, at each frequency bin. Figure 7 shows single-injection coupling functions for an accelerometer measured from shaker injections produced from three locations (the distribution of injection locations is discussed in Section 3.3. Since the injection locations are close
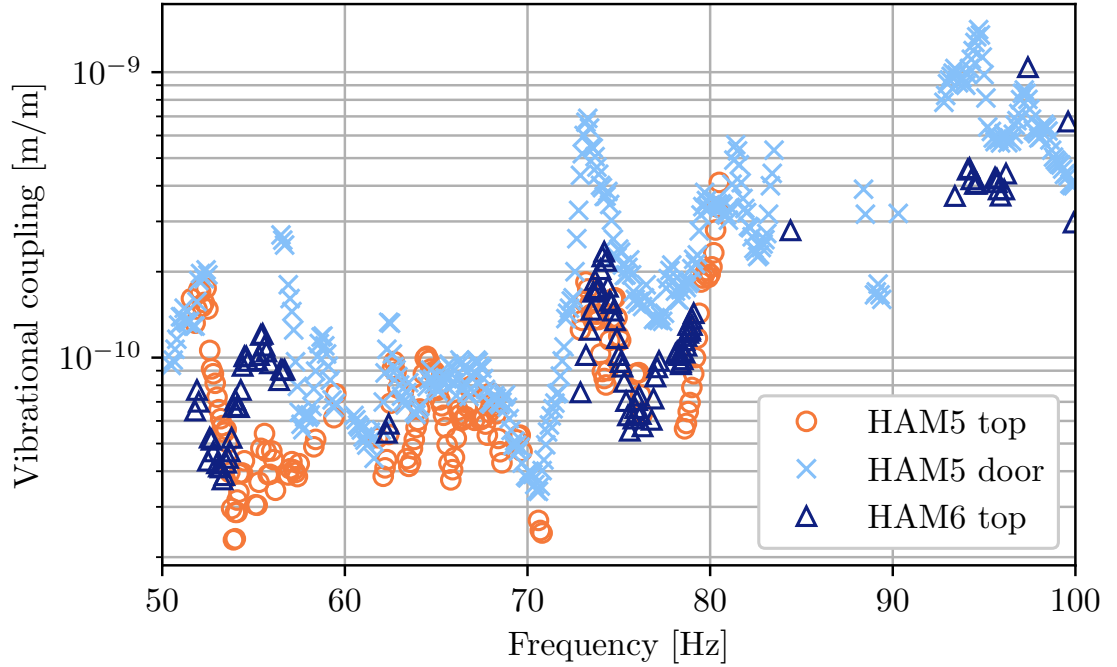
Figure 7. Single-injection coupling functions (upper limits not shown) for the HAM5 Y-axis accelerometer for three different shaker injection locations (on top of HAM5, on top of HAM6, and on the HAM5 chamber door).

enough to the accelerometer, it can be assumed that the variance is primarily due to finite spacing effect. Averaged across all frequency bins, the geometric standard deviation between injection locations is 1.4, i.e. coupling functions measured from vibrational injections can be expected to vary by a factor of 1.4 when measured by different injection locations.

Figure 8. Single-injection coupling functions (upper limits not shown) for various magnetometers and various injections at both observatories.

A similar study was performed combining geometric standard deviations for various magnetometers at both observatories. There are fewer magnetic injection locations to use for the comparison, but since coupling can be measured at each station (a corner station and both end stations) at each of the two LIGO observatories, there are twelve magnetometers that can be used, each

with two or more injections nearby. The result of this study is that magnetic coupling measurements and noise projections vary by a factor of 1.7.This is slightly greater than that of vibrational measurements, since the lower number of magnetometers means that the distances between coupling sites and sensors is greater, amplifying the finite spacing effect.

For both vibrational and magnetic coupling, these estimated uncertainties are acceptable given that conclusions made from coupling functions are often more qualitative than strictly quantitative, i.e. identifying and localizing coupling mechanisms is more important that precise estimates of the detector response. That said, more precise noise estimates may become important for quantifying the impact of environmental transients on GW event candidates, as discussed in Section 4.3.

Nodal artifacts from acoustic injections. In the case of acoustic injections, the uncertainty in a coupling function can be exacerbated when nodes and anti-nodes in the acoustic signal coincide with the location of a sensor but not a coupling site. This results in peaks and troughs in the sensor spectrum at frequencies that have a node or anti-node at the sensor location, respectively. These artifacts can impact any sensor, but are more noticeable in microphone spectra than accelerometer spectra, possibly because the stiffness of the vacuum enclosure results in effectively averaging over a larger area; in microphones, the peak-to-trough ratio is typically a factor of a few. The peaks and troughs are present in the sensor but not in the detector spectrum, because the sensor monitors a single point whereas the coupling to the interferometer is spread across a large enough area for the effects of nodes and anti-nodes to average out. Consequently, this effect imprints troughs and peaks onto the coupling function.

The artifacts can be smoothed out of the spectra by applying a moving average over $x_{ij,\text{inj}}(f)$ before computing $\mathcal{C}_{ij}(f)$. The moving average window must be on the scale of a few Hz since this is typically the scale of the peak-to-peak distances. On the other hand, smoothing of spectra can also result in less accurate coupling measurements when narrow mechanical resonances are present, so the window must balance the smoothing of artifacts against this disadvantage. For accelerometer spectra, analyzing injections with various smoothing parameters show that a logarithmically-scaled window which is XX Hz wide at $100\,\text{Hz}$ and XX Hz wide at $1000\,\text{Hz}$ best satisfy these constraints. Since microphones are much more sensitive to nodal artifacts while being less sensitive to narrow mechanical resonances (they would have to be strong enough to produce audible signals), their spectra can be smoothed much more aggressively: a logarithmically-scaled window is used which is $15\,\text{Hz}$ wide at $100\,\text{Hz}$ and $150\,\text{Hz}$ wide at $1000\,\text{Hz}$.

3.6 Tests of coupling functions

Pretty much just copied from PEM paper. Goal is to include most or all of the referenced calculations and figures here.

Although the injections used to measure coupling functions are designed to best replicate environmental noise, there are still differences and it is useful to test the coupling functions with different environmental events by comparing noise seen in the GW strain data during such events to noise levels predicted by PEM sensors and their coupling functions. Thunderstorms are known to produce short-duration transients in the strain data at tens of Hz. At LLO, coupling functions for several accelerometers at the Y end station, where

vibrational coupling was the highest, are capable of estimating the amplitude of multiple noise transients to within a factor two during a particularly loud thunderstorm.Helicopter flyovers can produce narrow-band features up to tens of seconds long. Coupling functions of various sensors at both observatories can predict the amplitudes of lines produced by multiple helicopter flyovers during O3 to within a factor of two in most cases.Long-duration noise due to vibrations from rain and the building heating, ventilation, and air conditioning (HVAC) is also well characterized by coupling functions at LHO.

3.7 The `pemcoupling` package

This section covers the technical details of the `pemcoupling` python package (Nguyen, 2020), which includes command-line tools for processing large numbers of injections and producing single-injection coupling functions, coupling functions, and multi-channel summary coupling functions.

The package uses the `gwpy` library for fetching raw time series data and producing ASDs of the GW strain channel and auxiliary channels from user-provided background and injection times.

3.7.1 Processing steps

This subsection is quite messy. The confusion comes from talking about different sensors at different steps. I think I could try splitting it by sensor type, like list all steps for accelerometers and microphones, then all steps for magnetometers.

A number of pre-processing steps are performed to condition the data for analysis. First, the auxiliary channel time series are examined for evidence

of saturation. Injections can cause saturation in two ways: actuator saturation due to overdriven amplifiers, or sensor saturation due to hitting the maximum amplitude the sensor can record.

During magnetic injections, the injection amplitude typically has to exceed background by a few orders of magnitude to produce noise in the GW channel, so comb magnetic injections are the most likely to saturate at the actuator. They are also capable of saturating the sensors if performed too close (such as in the electronics racks). In either case, intermodulation distortion occurs, generating peaks at sums and differences of the comb line frequencies while also reducing signal power in the injection lines. If the saturation is occuring at the actuator, the measured coupling is still accurate, but upper limits are higher due to the reduced signal power. On the other hand, sensor saturation results in inaccurate coupling measurements, because the line amplitudes no longer reflect the true magnetic signal at the sensor location.

Accelerometers can saturate in the presence of broadband vibrational injections. This results in artificial broadband noise in the amplitude spectra. The consequence is measuring a lower coupling function at frequencies where the saturation artifact dominates.

For these reasons, coupling functions are only measured for sensors that do not exceed 32,000 counts, as this is the sign of sensor saturation.

Once the time series are converted to ASDs, tri-axial magnetometer channels are combined in quadrature. Each magnetometer measures the x, y, and z components of its local magnetic field independently. An artificial channel is produced to represent the absolute magnitude of the field.

All PEM channels have accompanying calibration measurements (R. Schofield et al., 2021). Calibration for microphones and magnetometers is simply a constant conversion of Pa/count or T/count, respecitvely. Accelerometer ASDs are converted to acceleration (m/s^2), then to displacement (m) by dividing each bin by $(2\pi f)^2$ where f is the bin frequency.

For acoustic injections, spectral smoothing is applied at this point, in order to surpress nodal artifacts as explained in Section 3.5.3. Finally, the single-injection coupling funcitons $\mathcal{C}_{ij}(f)$ and upper limits $\mathcal{C}_{ul}(f)$ are measured as in eq. (3.7).

Paragraph or two on the CF calculation step.

3.7.2 Data products

For each $\mathcal{C}_{ij}(f)$, the data are saved in the following forms:

1. comma-separated text file consisting of data as described in Table **??**

2. plot of the raw coupling function (units of meters per analog-to-digital counts)

3. plot of the coupling function in physical units (meters per calibrated sensor unit, e.g. Tesla for magnetometers)

4. figure containing two subplots: one showing the background and injection spectra of the auxiliary sensor, and one showing the background and injection spectra of the GW strain data and the estimated environmental noise projection.

column	description
frequency	bin center frequency [Hz]
factor	coupling factor in [m/calibrated sensor unit]
factor_counts	coupling factor in [m/ADC count]
flag	"Measured", "Upper Limit", "Thresholds not met", or "No data"
sensINJ	sensor amplitude at injection time [calibrated sensor unit/Hz$^{1/2}$]
sensBG	sensor amplitude at background time [calibrated sensor unit/Hz$^{1/2}$]
darmINJ	GW channel amplitude at injection time [m/Hz$^{1/2}$]
darmBG	GW channel amplitude at background time [m/Hz$^{1/2}$]

Table 2. Column descriptions for the single-injection coupling function output of the `pemcoupling` package.

Post-processing, to aggregate single-injection coupling functions into coupling functions, and produce site-wide coupling plots, is done via additional commands, `pemcoupling-composite` and `pemcoupling-summary`.

Expand on these final steps a bit.

CHAPTER IV

STUDIES OF ENVIRONMENTAL NOISE DURING O3

Introduce how observing/engineering runs work, O3 schedule, etc.

O3 was preceded by an engineering run, a month-long period during
with the interferometer is operational at low-noise levels but not observing GW
events, to provide time for detector commissioning and noise studies.

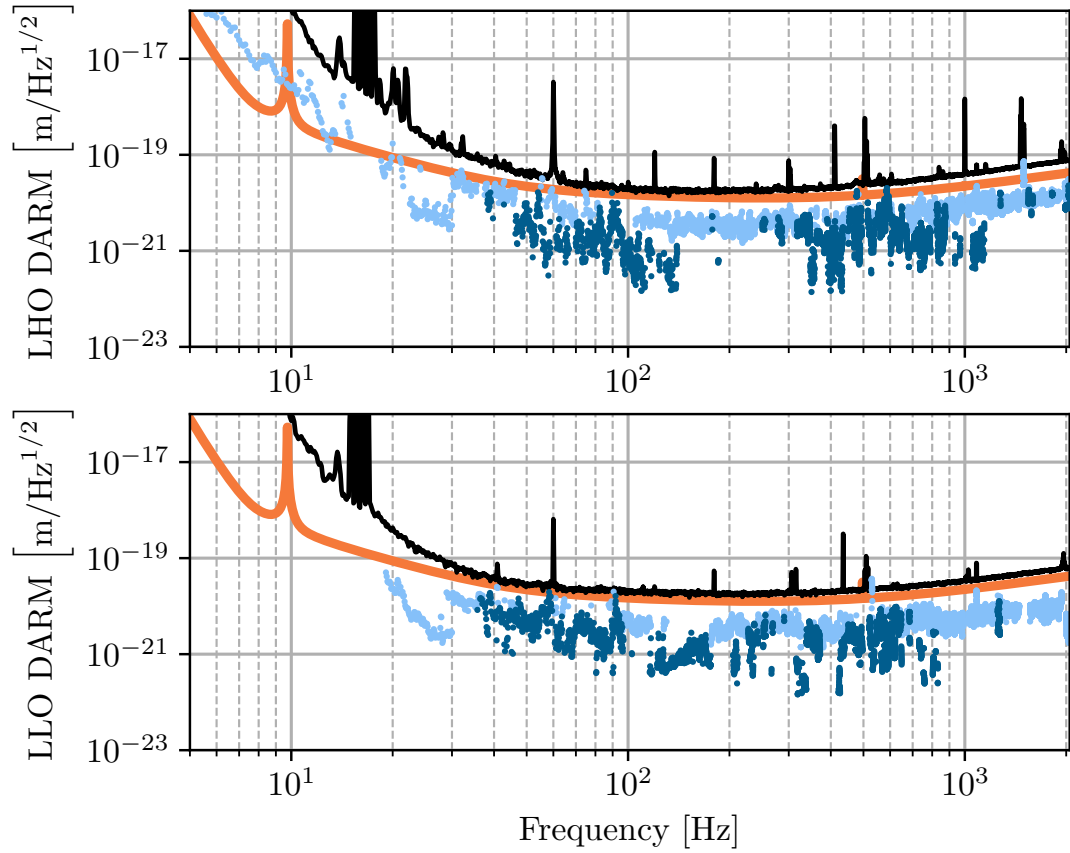## 4.1 Vibrational noise studies during O3

Figure 9. Ambient estimate of vibrational noise levels at LHO (top) and LLO
(bottom).

Figure 9 shows the ambient contribution of vibrational noise during O3, produced by combining the highest coupling factors among accelerometers and microphones measured from an injection campaign at the beginning of O3. At the end of O3, the vibration noise background at both observatories was dominated by input beam jitter above 100 Hz (discussed in Section **??**). At LHO, the dominant coupling region below 100 Hz was the output arm. At LLO, the dominant coupling regions were the Y-end in the 40-60 Hz band and the output arm in the 60-100 Hz band.

4.1.1 Scattered light at the HAM5/6 septum

A major source of detector noise and reduced sensitivity to GWs is the scattering of light from the beam spot on a test mass or other optic to surfaces that are moving relative to the optic, like vacuum chamber walls. A very small fraction of the light reaching the moving surface is reflected to the originating or another beam spot, where it scatters back into the main interferometer beam. As the distance to the moving surface changes, the phase of the returning light changes relative to the main beam, producing fluctuations in the amplitude of the beam, that, at 1 part in 10^{20} can be on the scale of those produced by gravitational waves. In addition to this sensitivity to recombined scattered light, the scattering noise is problematic because of non-linear coupling when the path length modulation becomes comparable to the wavelength of the light, producing noise at harmonics of modulation frequencies (Soni et al., 2020).

At LHO, investigations throughout O3 showed that scattering noise produces noise near the detector noise background in the frequency range of 38–100 Hz. The sensors with the highest ambient projections in this band were

accelerometers located on the HAM 5 and HAM 6 vacuum chambers, which contain the GW channel readout, as well as the optics of the output mode cleaner, squeezed light system, and signal recycling cavity. The coupling was excited most strongly by injections around the output arm, but acoustic noise produced as far as the Y-arm manifold $\approx 50\,\mathrm{m}$ away produced excess noise in DARM. Spectra from the nearest injections also show non-linear coupling behavior (Expand on this). Shaker injections were also performed throughout the corner station, confirming that the dominant coupling site was in the HAM 5 and 6 area. Nonlin This evidence suggested that the coupling was caused by scattered light within HAM 5 or HAM 6. A more thorough investigation was required to localize the exact scattering surface.

Figure 10 shows time series and spectrograms of a single impulse injection performed in the horizontal access module (HAM) 5/6 area. The plots show a single impulse injection signal in the GW channel and in various output optics accelerometers. Multiple sensors observe an impulse time-of-arrival matching that of the GW channel, but repeating the injection from various other locations rules out sensors that do not match it consistently across multiple injections. In this case the septum (separating the HAM5 and HAM6 chambers) accelerometer signal matches the DARM signal most consistently (other injections not shown for brevity).

Spectrograms of the same impulse injection for DARM and the three sensors with the closest matching time-of-arrival to that of DARM reveals similarities between the frequency structure of the septum accelerometer signal and that of DARM. This provides further support that the septum is the dominant coupling site in the output arm.
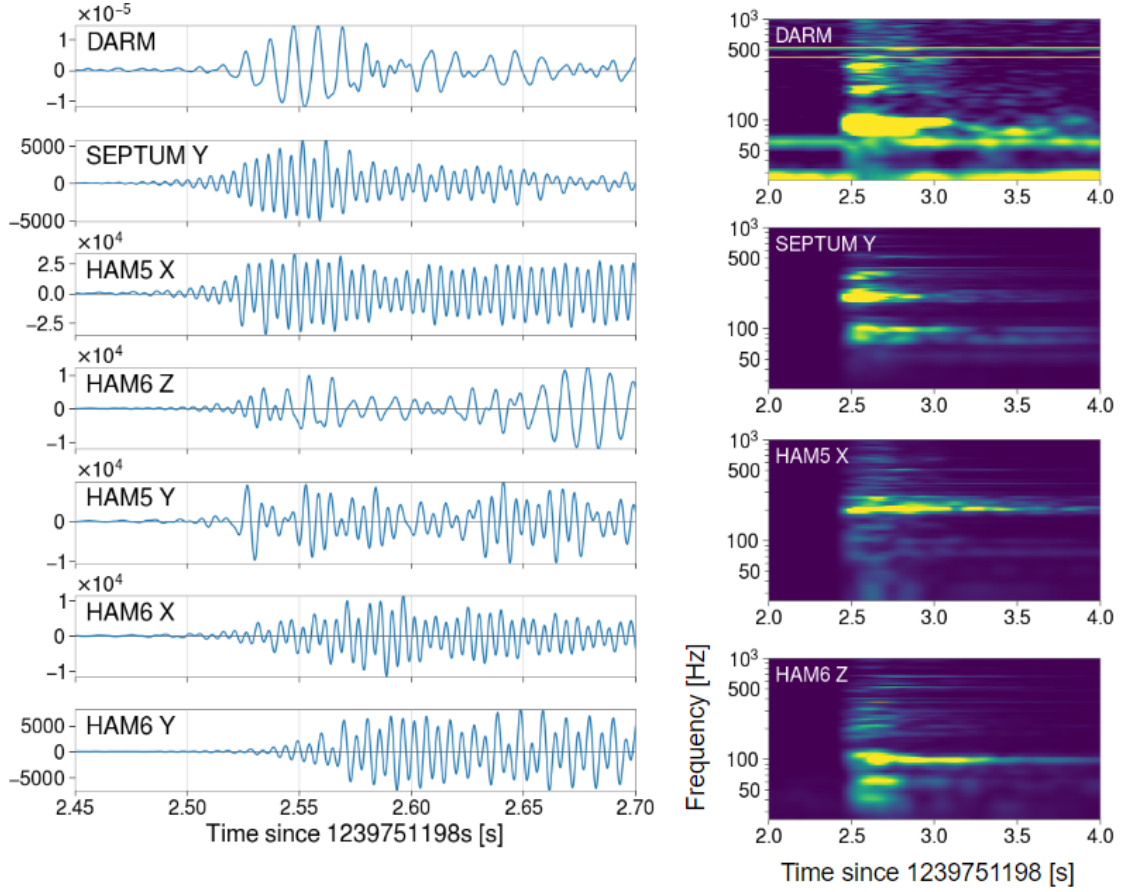
Figure 10. Time series (left) and spectrograms (right) of a vibrational impulse injection produced at the output arm of the LHO detector.

4.1.2 Search for the source of a 48-Hz peak

Figure 11 shows spectrograms of a beating-shakers injection used to localize the coupling site responsible for a 48-Hz noise peak in the DARM spectrum. The shakers were injecting at 48 and 48.01 Hz. The Y-axes of the spectrograms are centered along at 48 Hz and show the combined signal in each sensor modulating at the beat frequency (0.01 Hz). This set of spectrograms suggests that the accelerometers on the input test mass (ITM) chambers and the Y-axis HAM2 accelerometer are likely not close to the true coupling location,

since the beat envelopes are the furthest offset from the beat envelope in the DARM response.
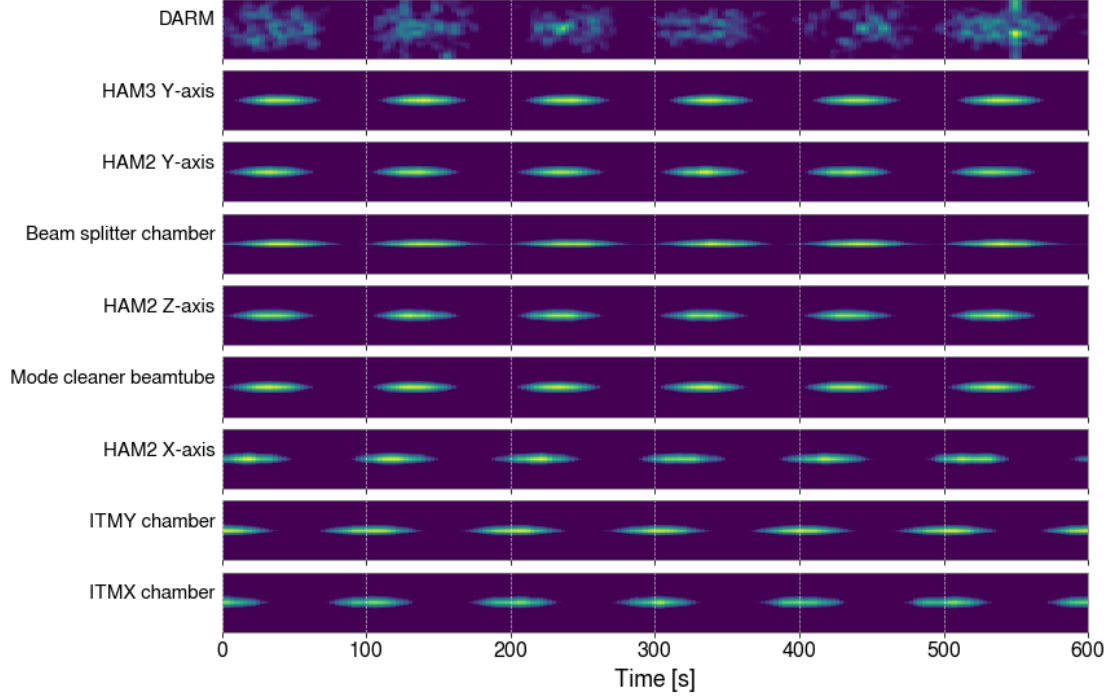
Figure 11. Spectrograms of DARM and various accelerometers near the input arm and beam splitter showing a beating-shakers injection at 48 Hz.

Multiple other injections were made (not shown here) with varying shaker locations in order to rule out other sensors until the most likely candidate remaining was the HAM3 Y-axis accelerometer. Black glass was used to block scattered light at this location and the peak was eliminated for the second half of the O3 observation run. Figure 12 shows the noise reduction in the GW channel after the light scattering was mitigated.

4.1.3   Input beam jitter

Short discussion, summarize measurements and improvement. Will make sure to discuss impact of test mass defect on jitter noise.
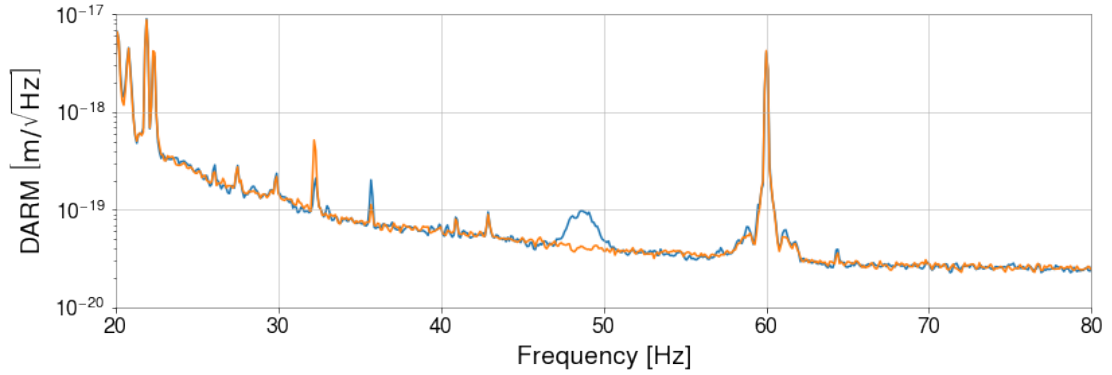
Figure 12. LHO DARM spectrum before and after mitigation of the 48-Hz peak.

Figure 13. Improvement in jitter coupling at LHO (left) and LLO (right) between the start and end of O3.

4.2   Magnetic noise studies during O3

Magnetic injections early in aLIGO suggested that coupling to permanent magnets in the suspension system could prevent LIGO from reaching design sensitivity in the 10-20 Hz regions (R. M. S. Schofield, 2013). While the test mass actuator is electrostatic and not magnetic (as in iLIGO), a number of permanent magnets were used in the suspensions, including for actuation in the first three of the four levels of the isolation chain and for eddy current damping. The greatest number of permanent magnets were in the eddy current damping arrays and these were removed. Nevertheless, ambient fields are still predicted to produce noise at greater than one-tenth of the design sensitivity in the 10-20 Hz band (Figure 14), and may need to be further addressed as we reach design sensitivity in the 10 Hz region.

At higher frequencies, generally above about 30 Hz, the dominant magnetic coupling appears to be through induction of currents in cables and at connectors, mainly to actuator cabling and other cabling in the control system.
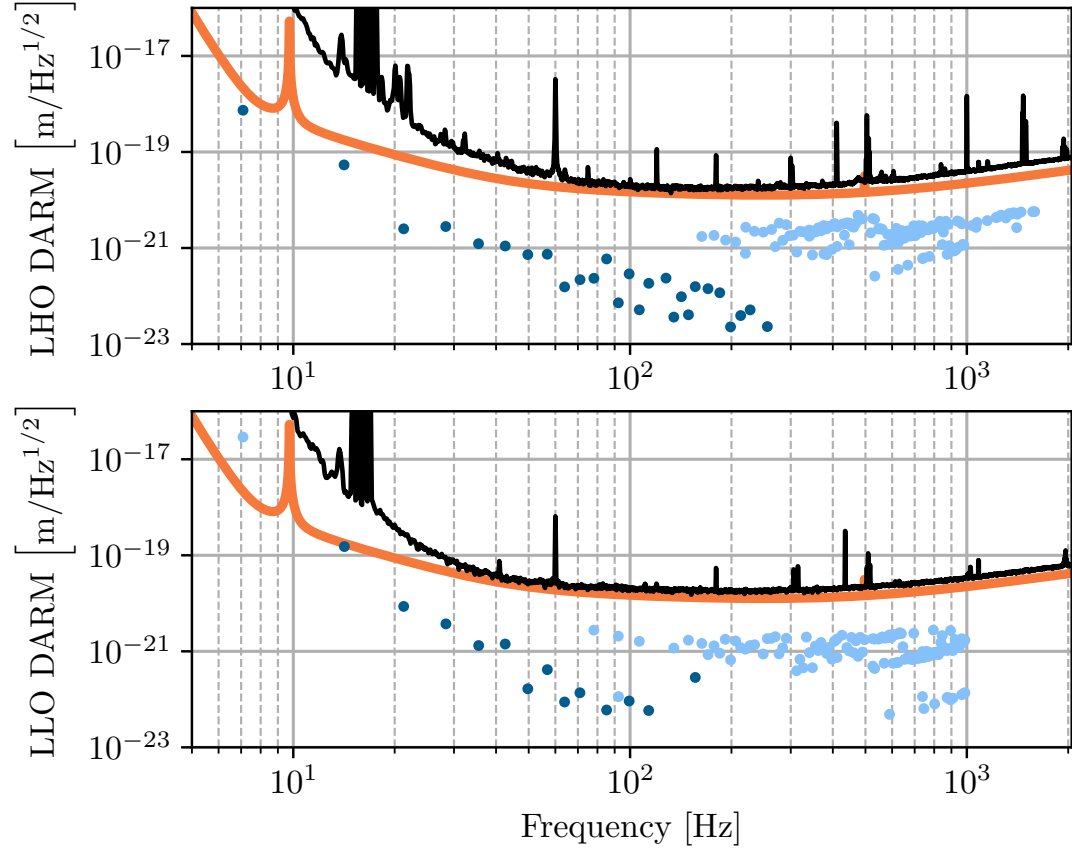
Figure 14. Ambient estimate of magnetic noise levels at LHO (top) and LLO (bottom).

Mitigation of coupling to cables and connectors has required a continuing program of monitoring coupling since cables are often disconnected and reconnected during runs as electronics are replaced for problems or upgrades. This program consists of making weekly, broadband magnetic field injections using the large wall-mounted coils described in Section 3.3.2. The injections have shown that peaks can appear or disappear, as well as shift in frequency, on a weekly basis.

Figure 15. Ambient estimate of magnetic noise levels at LHO on Mar XX, 2019 (blue), XX weeks before O3, and on Apr XX, 2019 (orange), XX weeks into O3.

Figure 16. Weekly trends in frequency (top) and amplitude (top) of peaks in the magnetic coupling functions.

4.2.1 Fluctuations in magnetic coupling

4.3 Validation of gravitational wave event candidates

In addition to investigating sources of environmental influences, knowledge acquired from environmental studies contributes to the vetting of GW event candidates. Analysis pipelines search the strain data for astrophysical signals. They are categorized into modeled searches for binary mergers that match the data to template waveforms (e.g. GstLAL (Cannon et al., 2012) and PyCBC (Usman et al., 2016)) and un-modeled searches that identify excess energy coherent between multiple detectors (e.g. cWB (Klimenko, Yakushin, Mercer, & Mitselmakher, 2008), oLIB (Lynch, Vitale, Essick, Katsavounidis, & Robinet, 2017), and BW (Cornish & Littenberg, 2015)).

Contamination of the GW data can occur through any of the means discussed in previous sections. Environmental noise has the potential to be correlated between detectors by stemming from a common source, such as through electromagnetic signals from distant sources or glitches in GPS-correlated electronics. The analysis pipelines estimate the false-alarm probabilities for GW events based on the background rate of randomly coincident events in the detector network. They generate background events by time-shifting the data stream of one detector relative to another by time steps much longer than the light travel time between detectors and longer

than the duration of GW signals.This method does not account for the possibility of transients being correlated between the detectors due to a common environmental source.

Environmental noise is also particularly relevant to un-modeled searches. Unlike template-based methods, these searches make minimal assumptions about the signal waveform and rely more heavily on signal correlation between sites.

The first observation of a GW occurred on 14 Sept 2015 (Abbott et al., 2016b). The event, a short-duration binary black hole merger designated GW150914, required a number of follow-up investigations to find potential noise sources around the time of the event (Abbott et al., 2016a). This included an examination of the status of all PEM sensors and any significant signals they observed for possible contamination of the GW signal (R. M. S. Schofield, Roma, et al., 2018). A few of the PEM sensors were not working, but because of redundancy, coverage was sufficient.

Comparisons between Q-transform spectrograms (Chatterji, Blackburn, Martin, & Katsavounidis, 2004) of all coincident events in environmental sensors to the time-frequency path of the event revealed that no environmental signals had paths similar to the event candidate. Q-transforms produce a quality-factor-optimized logarithmic tiling of the time-frequency space, making them useful for visualizing transients. The signal-to-noise ratios (SNRs) of the matching signals were also compared to that of the event, showing that even if there were overlapping time-frequency paths, none of the environmental signals were large enough to influence the strain data at the SNR level of the event, based on multiplying the environmental signals by their respective sensor coupling functions.

The validation process for novel events such as GW150914 also includes redundant checks for global sources of environmental noise. We use a dedicated cosmic ray detector located below an input test mass at LHO to examine any association of cosmic ray showers to excess noise in DARM. We also check external observatories for coronal mass ejections, solar radio signals, geomagnetic signals, and radio-frequency (RF) signals in the detection band as well as higher frequencies.

There was specific concern over a co-incident extremely-high current (504 kA) lightning strike over Burkina Faso, prompting additional studies of the effects of lightning on the interferometer (R. M. S. Schofield, 2018). Investigations of similar strikes found no effect on the strain data and investigations of closer strikes confirmed that the magnetometers were much more sensitive to lightning strikes than the interferometer was. In conclusion there was no reason to veto the first detection based on environmental disturbances.

Subsequent detections throughout O1 and O2 employed a similar procedure; however the development of the method described in Section 3.4 for producing coupling functions for all sensors expedited the process. This was especially important for examining environmental noise during GW170817, the first long-duration event detected by LIGO (B. P. Abbott et al., 2017; R. M. S. Schofield, Nguyen, et al., 2018). The longer duration of this event (75 s) unsurprisingly overlapped with many environmental signals. Based on the coupling functions for those sensors, several of these environmental events were loud enough (estimated DARM signals of up to SNR 4) to have contributed to the interferometer readout, but not enough to account for the GW signal.

Furthermore, none of them had a time-frequency morphology that correlated with any features in the candidate signal.

4.3.1 Automated event validation

Since the start of O3, most of the procedure described above has been automated in order to handle the increase in detection rate. The automated vetting is performed by the `pemcheck` routine, which is a part of the Data Quality Report (DQR). When an event is detected by the astrophysical search pipelines, a DQR is initiated and assembles a plethora of tasks for assessing the data quality at each observatory during the time of the event. Among these tasks, an omega scan pipeline (Chatterji et al., 2004; Davis et al., 2021) is used to search for transient noise in all PEM sensors in the time window spanning the event candidate. It does so by producing a Q-transform for each sensor and reporting those in which there is a transient signal with a false-alarm rate below 10^{-3} Hz. The omega scan also reports the frequency and amplitude of the most significant tile for each sensor. The `pemcheck` in O3 used the output of the omega scan to estimate each sensor's potential affect on the data quality of the detector. The coupling function of each sensor was interpolated at the peak frequency and multiplied by the peak amplitude, producing an estimated DARM amplitude.

Sensors whose estimated contribution exceed one tenth of the DARM background level were flagged for human input, requiring a comparison of the environmental signal morphology to that of the event candidate. If there was sufficient signal overlap, reviewers may advise that analysts perform some noise removal in the data, such as by gating or filtering out the appropriate time or

frequency range, before performing further follow up analyses. The event could be retracted, if gating or filtering out the environmental contribution would reduce the signal-to-noise ratio of the candidate to a level no longer consistent with a GW detection.

During O3, no candidates were retracted on the basis of the environmental coupling check alone. Some human input was still required for all of the XX events reported in (R. Abbott et al., 2021a), although little to no signal overlap of environmental transients was seen.

4.3.2   Event validation in O4

With the GW detection rate expected to increase in O4, a more sophisticated and streamlined vetting routine is necessary. The DQR in O4 will report a p-value for each vetting task, including the `pemcheck` task. In the case of environmental noise vetting, this p-value represents the null-hypothesis probability, i.e. the probability that environmental disturbances are not contaminating the GW event signal. This probability is defined based on the uncertainty of the coupling functions. The coupling in a single frequency bin is described by a log-normal probability distribution with $\mu = \log C(f_k)$ and $\sigma^2 = 1$, if $C(f_k)$ is a measurement:

$$P(x) = \text{LogNormal}(\mu, \sigma^2) = \frac{1}{x\sigma\sqrt{2\pi}} \exp\left(-\frac{(\ln(x) - \mu^2)}{2\sigma^2}\right) \qquad (4.1)$$

If $C(f_k)$ is an upper limit, then the coupling is assumed to be equal to or less than $C(f_k)$, so it is described by the uniform probability distribution

$$P(x) = \begin{cases} \frac{1}{C(f_k)} & \text{if } x < C(f_k) \\ 0 & \text{otherwise} \end{cases} \qquad (4.2)$$

CHAPTER V

GRAVITATIONAL WAVES ASSOCIATED WITH GAMMA-RAY BURSTS

5.1 Gamma-ray bursts

Gamma-ray bursts (GRBs) are short, energetic bursts of gamma rays in the MeV range, first discovered in 1967 (Klebesadel, Strong, & Olson, 1973). Observations throughout the following decades revealed that GRBs could be classified based on duration and spectral hardness (Kouveliotou et al., 1993). This classification has become the most used to describe GRBs: long-soft bursts last $\gtrsim$ 2 s and have soft emission spectra, i.e. lacking in higher energy photons, while short-hard bursts last $\lesssim$ 2 s and had harder emission spectra. It is believed that the ultra-relativstic jets required to produce GRBs come from either black holes (Woosley, 1993) or magnetars (Dai & Lu, 1998).

A multitude of models have been proposed throughout the decades to explain the origins of GRBs.

Photometry and spectroscopy data provide evidence that long GRBs originate from core-collapse supernovae (CCSNe), whereas short GRBs are believed to be associated with compact binary mergers, such as the BNS merger GW170817 (B. P. Abbott et al., 2017).

5.2 GW searches

In 2017, the first binary neutron star merger GW170817 was detected by advanced LIGO and Virgo, immediately accompanied by the detection of a relatively low-luminosity gamma-ray burst GRB170817A by Fermi Gamma-ray Burst Monitor (GBM) two seconds later (B. P. Abbott et al., 2017). This prompted a global effort to find an optical, UV, and infrared counterpart that

would make up the signature of a kilonova. The localization provided by the joint detection was sufficient to locate a counterpart near NGC 4993.

GW parameter estimation suffers from a degeneracy between distance and orbital plane inclination; increasing the distance of the merger and orienting its orbital plane would both result in a lower GW amplitude. This degeneracy can be broken if either one could be measured externally. If the joint detection localization were good enough to determine a host galaxy, this would greatly help resolve the distance, however this will more likely require observation of an optical or UV counterpart due to the poor localization provided by current GRB and GW detectors. In the case of GW170817, the host galaxy whose redshift was known was used to determine the distance, which then allowed for a more precise measurement of the inclination angle. A separate analysis using the distance measured from the GW detection combined with the known redshift made the first joint GW-EM measurement of the Hubble constant, albeit with very large uncertainty due to the small sample size (Abbott et al., 2017).

One of the many unanswered questions surrounding GRBs pertains to their jet profile, the luminosity as a function of viewing angle (the angle between the observer and the symmetric axis of the jet; the profile is assumed to be axially symmetric and independent of distance). When information about the jet profile is required, e.g. for making rate estimates for GRB detections, the profile is typically modeled as a top-hat (uniform within some opening angle and dropping sharply beyond it) for simplicity, but the true profile may be different.

Determining the viewing angle θ_{obs} of a GRB is essential for distinguishing between different jet profile models, but it relies on the ability to observe an afterglow emission. These emissions, ranging from radio to X-

rays, follow the prompt emission of γ-rays and are generated by the interaction between the relativistic outflow and the surrounding medium. The observation of these afterglows was crucial in improving localization of the GRB sources and provided valuable information about the energy scale of the jet, as well as measurements of θ_{obs}. The latter came from observing the signature jet break in the afterglow light curve, resulting from the lateral spreading of jet material as it expands; the opening angle can be determined from the timing of the jet break. However, few jet breaks have been observed for short GRBs, so existing observations do not place tight constraints on opening angle (Biscoveanu, Thrane, & Vitale, 2020).

Joint GW-GRB observations can provide much more information on jet properties (Farah et al., 2020; Mogushi, Cavaglià, & Siellez, 2019). GRB170817 was orders of magnitude less energetic than most short GRBs, so it likely would have been ignored in the absense of a GW coincidence. Its low luminosity immediately ruled out an on-axis top-hat jet. An off-axis top-hat jet was considered unlikely as well because the narrow opening angle predicted for top-hat jets based on theory and past GRB measurements only allowed for $\theta_{\mathrm{obs}} \lesssim 10 \deg$. More evidence against an off-axis top-hat model arose when the bright afterglow expected to emerge after ~ 1 day was not observed. These observations instead favored a wide-angled, structured jet model for GRB170817. A structured jet model may refer to any luminosity function that decreases gradually with θ_{obs} rather than abruptly, e.g. a Gaussian or power-law with uniform center. One mechanism that would explain such a model is a cocoon emission, in which the relativistic jet interacts dissipatively with the surrounding

merger ejecta, depositing its energy into a cocoon fireball that results in a structured jet (B. P. Abbott et al., 2017).

5.2.1 X-Pipeline

5.3 O3 search for GWs associated with GRBs

5.3.1 GRB sample

5.3.2 Results

5.3.3 Noise assessment

REFERENCES CITED

Abbott, B. P., Abbott, R., Abbott, T. D., Acernese, F., Ackley, K., Adams, C.,
... et al. (2017, Oct). Gravitational waves and gamma-rays from a
binary neutron star merger: Gw170817 and grb 170817a. ApJ, *848*(2),
L13. Retrieved from `http://dx.doi.org/10.3847/2041-8213/aa920c`
doi: 10.3847/2041-8213/aa920c

Abbott, B. P., et al. (2016a, Jun). Characterization of transient noise in
Advanced LIGO relevant to gravitational wave signal GW150914. *Class.
Quantum Grav.*, *33*(13), 134001.

Abbott, B. P., et al. (2016b, Feb). Observation of gravitational waves from a
binary black hole merger. *Phys. Rev. Lett.*, *116*, 061102.

Abbott, B. P., et al. (2017, November). A gravitational-wave standard siren
measurement of the Hubble constant. Nature, *551*(7678), 85-88. doi:
10.1038/nature24471

Abbott, B. P., et al. (2017, Oct). GW170817: Observation of gravitational waves
from a binary neutron star inspiral. *Phys. Rev. Lett.*, *119*, 161101.

Abbott, B. P., et al. (2019, Sep). GWTC-1: A gravitational-wave transient
catalog of compact binary mergers observed by LIGO and Virgo during
the first and second observing runs. *Phys. Rev. X*, *9*, 031040. Retrieved
from `https://link.aps.org/doi/10.1103/PhysRevX.9.031040` doi:
10.1103/PhysRevX.9.031040

Abbott, R., et al. (2021a, Jun). Gwtc-2: Compact binary coalescences observed
by ligo and virgo during the first half of the third observing run. *Phys.
Rev. X*, *11*, 021053. Retrieved from
`https://link.aps.org/doi/10.1103/PhysRevX.11.021053` doi:
10.1103/PhysRevX.11.021053

Abbott, R., et al. (2021b). GWTC-3: Compact binary coalescences observed by
LIGO and Virgo during the second part of the third observing run.

APS Dynamics. (2014, Mar). *APS 113 ELECTRO-SEIS Long Stroke Shaker.*
`https://www.apsdynamics.com/en/products/details/`
`vibration-exciter/aps-113-ab.html?file=files/spektra_relaunch/`
`inhalte/produktgruppen/datenblaetter/`
`APS_113-AB_AB-HF_Data_Sheet_en.pdf`.

Biscoveanu, S., Thrane, E., & Vitale, S. (2020, April). Constraining Short Gamma-Ray Burst Jet Properties with Gravitational Waves and Gamma-Rays. ApJ, *893*(1), 38. doi: 10.3847/1538-4357/ab7eaf

Brüel & Kjær. (2021, Jun). *Type 4809 portable shaker/vibration exciter .* `https://www.bksv.com/-/media/literature/Product-Data/bp0231.ashx`.

Buikema, A., et al. (2020, Sep). Sensitivity and performance of the Advanced LIGO detectors in the third observing run. *Phys. Rev. D*, *102*, 062003.

Cannon, K., et al. (2012, March). Toward early-warning detetion of gravitational waves from copmact binary coalescence. *Astrophys. J.*, *748*(2), 136.

Chatterji, S., Blackburn, L., Martin, G., & Katsavounidis, E. (2004, sep). Multiresolution techniques for the detection of gravitational-wave bursts. *Class. Quantum Grav.*, *21*(20), S1809–S1818.

Christensen, N. (2018, Nov). Stochastic gravitational wave backgrounds. *Reports on Progress in Physics*, *82*(1), 016903. Retrieved from `https://doi.org/10.1088/1361-6633/aae6b5` doi: 10.1088/1361-6633/aae6b5

Cornish, N. J., & Littenberg, T. B. (2015, June). Bayeswave: Bayesian inference for gravitational wave bursts and instrument glitches. *Class. Quantum Grav.*, *32*(13), 135012.

Creighton, J. D. E., & Anderson, W. G. (2011). *Gravitational-wave physics and astronomy.* Wiley-VCH.

Dai, Z. G., & Lu, T. (1998, May). Gamma-ray burst afterglows and evolution of postburst fireballs with energy injection from strongly magnetic millisecond pulsars. A&A, *333*, L87-L90.

Davis, D., et al. (2021, Apr). LIGO detector characterization in the second and third observing runs. *Class. Quantum Grav.*, *38*(13), 135014. Retrieved from `https://doi.org/10.1088/1361-6382/abfd85` doi: 10.1088/1361-6382/abfd85

Effler, A., Schofield, R. M. S., Frolov, V. V., González, G., Kawabe, K., Smith, J. R., . . . McCarthy, R. (2015, Jan). Environmental influences on the LIGO gravitational wave detectors during the 6th science run. *Class. Quantum Grav.*, *32*(3), 035017. doi: 10.1088/0264-9381/32/3/035017

Farah, A., et al. (2020, June). Counting on Short Gamma-Ray Bursts: Gravitational-Wave Constraints of Jet Geometry. ApJ, *895*(2), 108. doi: 10.3847/1538-4357/ab8d26

Klebesadel, R. W., Strong, I. B., & Olson, R. A. (1973, June). Observations of Gamma-Ray Bursts of Cosmic Origin. ApJ, *182*, L85. doi: 10.1086/181225

Klimenko, S., Yakushin, I., Mercer, A., & Mitselmakher, G. (2008, May). A coherent method for detection of gravitational wave bursts. *Class. Quantum Grav.*, *25*(11), 114029.

Kouveliotou, C., Meegan, C. A., Fishman, G. J., Bhat, N. P., Briggs, M. S., Koshut, T. M., ... Pendleton, G. N. (1993, August). Identification of Two Classes of Gamma-Ray Bursts. ApJ, *413*, L101. doi: 10.1086/186969

Kruk, J., & Schofield, R. M. S. (2016, Aug). *Environmental Monitoring: Coupling Function Calculator.* `https://dcc.ligo.org/LIGO-T1600387/public`. LIGO Document Control Center.

Lynch, R., Vitale, S., Essick, R., Katsavounidis, E., & Robinet, F. (2017, May). Information-theoretic approach to the gravitational-wave burst detection problem. *Phys. Rev. D*, *95*, 104046.

Mogushi, K., Cavaglià, M., & Siellez, K. (2019, Jul). Jet geometry and rate estimate of coincident gamma-ray burst and gravitational-wave observations. ApJ, *880*(1), 55. Retrieved from `http://dx.doi.org/10.3847/1538-4357/ab1f76` doi: 10.3847/1538-4357/ab1f76

Nguyen, P. (2020, Apr). *PEM Coupling Function Tools.* `https://git.ligo.org/philippe.nguyen/pemcoupling`. GitHub.

Nguyen, P., et al. (2021, jun). Environmental noise in Advanced LIGO detectors. *Class. Quantum Grav.*, *38*(14), 145001. Retrieved from `https://doi.org/10.1088/1361-6382/ac011a` doi: 10.1088/1361-6382/ac011a

Piezosystems. (n.d.). *Piezo nanopositioning devices, actuators & controllers.* `https://www.piezosystem.com/`.

Riles, K. (2017, Dec). Recent searches for continuous gravitational waves. *Modern Physics Letters A*, *32*(39), 1730035. Retrieved from `http://dx.doi.org/10.1142/S021773231730035X` doi: 10.1142/s02177323173035x

Schofield, R., Effler, A., Nguyen, P., et al. (2021). *PEM central.* `http://pem.ligo.org`.

Schofield, R. M. S. (2013, Mar). *Investigations of magnetic coupling to the quads.* `https://dcc.ligo.org/LIGO-G1300300/public`. LIGO Document Control Center.

Schofield, R. M. S. (2018, Nov). *Lightning, LIGO, and GW150914.* `https://dcc.ligo.org/LIGO-T1800506/public`. LIGO Document Control Center.

Schofield, R. M. S., Nguyen, P., Roma, V., Palamos, J., Schale, P., Effler, A., ... Frey, R. (2018, Nov). *PEM vetting report for GW170817.* `https://dcc.ligo.org/LIGO-T1800508/public`. LIGO Document Control Center.

Schofield, R. M. S., Roma, V., Palamos, J., Hardwick, T., Effler, A., Frey, R., & Talukder, D. (2018, Nov). *PEM vetting report for GW150914.* `https://dcc.ligo.org/LIGO-T1800505/public`. LIGO Document Control Center.

Soni, S., et al. (2020, Dec). Reducing scattered light in LIGO's third observing run. *Class. Quantum Grav.*, *38*(02), 025016.

Usman, S., et al. (2016, October). The PyCBC search for gravitational waves from compact binary coalescence. *Class. Quantum Grav.*, *33*(21), 215004.

Woosley, S. E. (1993, March). Gamma-Ray Bursts from Stellar Mass Accretion Disks around Black Holes. ApJ, *405*, 273. doi: 10.1086/172359